Fundamental parameters of 16 late-type stars derived from their angular diameter measured with VLTI/AMBER[*]

P. Cruzalèbes,[1]† A. Jorissen,[2] Y. Rabbia,[1] S. Sacuto,[3,4] A. Chiavassa,[1,2] E. Pasquato,[2] B. Plez,[5] K. Eriksson,[3] A. Spang[1] and O. Chesneau[1]

[1]*Laboratoire Lagrange, UMR 7293, Université de Nice-Sophia Antipolis, CNRS, Observatoire de la Côte d'Azur, Bd de l'Observatoire, B.P. 4229, F-06304 Nice cedex 4, France*
[2]*Institut d'Astronomie et d'Astrophysique, Université Libre de Bruxelles, Campus Plaine C.P. 226, Bd du Triomphe, B-1050 Bruxelles, Belgium*
[3]*Department of Astronomy and Space Physics, Uppsala Astronomical Observatory, Box 515, S-751 20 Uppsala, Sweden*
[4]*Institute of Astronomy, University of Vienna, Türkenschanzstraße 17, A-1180 Vienna, Austria*
[5]*Laboratoire Univers et Particules, Université Montpellier II, CNRS, F-34095 Montpellier cedex 5, France*

ABSTRACT

Thanks to their large angular dimension and brightness, red giants and supergiants are privileged targets for optical long-baseline interferometers. 16 red giants and supergiants have been observed with the VLTI/AMBER facility over a 2-year period, at medium spectral resolution ($\mathcal{R} = 1500$) in the K band. The limb-darkened angular diameters are derived from fits of stellar atmospheric models on the visibility and the triple product data. The angular diameters do not show any significant temporal variation, except for one target: TX Psc, which shows a variation of 4 per cent using visibility data. For the eight targets previously measured by long-baseline interferometry (LBI) in the same spectral range, the difference between our diameters and the literature values is less than 5 per cent, except for TX Psc, which shows a difference of 11 per cent. For the eight other targets, the present angular diameters are the first measured from LBI. Angular diameters are then used to determine several fundamental stellar parameters, and to locate these targets in the Hertzsprung–Russell diagram (HRD). Except for the enigmatic Tc-poor low-mass carbon star W Ori, the location of Tc-rich stars in the HRD matches remarkably well the thermally-pulsating asymptotic giant branch, as it is predicted by the stellar evolution models. For pulsating stars with periods available, we compute the pulsation constant and locate the stars along the various sequences in the period–luminosity diagram. We confirm the increase in mass along the pulsation sequences, as predicted by theory, except for W Ori which, despite being less massive, appears to have a longer period than T Cet along the first-overtone sequence.

Key words: methods: data analysis – techniques: interferometric – stars: atmospheres – stars: fundamental parameters – stars: late-type.

1 INTRODUCTION

The direct measurement of stellar angular diameters has been the principal goal of most attempts with astronomical interferometers since the pioneering work of Michelson & Pease (1921). For stars of known distance, the angular diameter ϕ, combined with the parallax ϖ, yields the stellar radius $\mathcal{R} = 0.5\phi/\varpi$, where R is in au. When combined with the emergent flux at the stellar surface, linked to the effective temperature $T_{\rm eff}$, the stellar radius $\mathcal{R}$ leads to the absolute luminosity $\mathcal{L} = 4\pi\mathcal{R}^2\sigma T_{\rm eff}^4$, where σ is the Stefan–Boltzmann constant.

These quantities are essential links between the observed properties of stars and the results of theoretical calculations on stellar structures and atmospheres (Baschek, Scholz & Wehrse 1991; Scholz 1997; Dumm & Schild 1998).

Because of their comparatively large dimension, late-type giants and supergiants are suitable targets for modern Michelson interferometers, reaching accuracies better than a few per cent (see e.g. van Belle et al. 1996; Millan-Gabet et al. 2005). With radii larger than 1 au, many nearby giants subtend relatively large angular

diameters (>20 mas at 100 pc). They also have high brightnesses in the near-infrared, allowing interferometric measurements with high signal-to-noise ratio (SNR).

Using the ESO/VLTI facility, we initiated in 2009 a long-term programme with the ultimate goal of investigating the presence of surface brightness asymmetries (SBAs), and of their temporal behaviour, following the pioneering work of Ragland et al. (2006). This issue is addressed in a companion paper (Cruzalèbes et al. 2013b). The AMBER instrument is well suited for that purpose, since it provides phase closures at medium spectral resolution in *K*. This goal prompted us to select our targets all over the red-giant and supergiant regions of the Hertzsprung–Russell diagram (HRD). Investigation of SBAs is important in the framework of the *GAIA* astrometric satellite (Perryman et al. 2001; Lindegren et al. 2008), since the presence of time-variable SBAs may hinder its ability to derive accurate parallaxes for such stars (see the discussions by Bastian & Hefele 2005; Eriksson & Lindegren 2007; Pasquato, Pourbaix & Jorissen 2011; Chiavassa et al. 2011).

In this paper, we present new determinations of the angular diameters of 16 red giants and supergiants, obtained by combining the fits of limb-darkened disc models using two SPectro-Interferometric (SPI) observables: the visibility amplitude and the triple product. The visibility is defined as the ratio of the modulus of the coherent to the incoherent flux and the triple product as the ratio of the bispectrum to the cubed incoherent flux (see Cruzalèbes et al. 2013a for details). In Section 2, we describe the measurement technique, and the sample of observed sources; in Section 3, we describe the model-fitting procedure; in Section 4, we study the sensitivity of our results with respect to the fundamental parameters of the model: linear radius, effective temperature, surface gravity and microturbulence velocity; in Section 5, we study the possible temporal variability of the angular diameter; in Section 6, we describe the method for deriving the final angular diameter; in Section 7, we confront our results with those of the literature.

Then, our stellar radii are used to infer various fundamental stellar characteristics: (i) location in the HRD, and masses derived from a comparison with evolutionary tracks (Section 8); (ii) luminosity threshold for the occurrence of technetium on the asymptotic giant branch (AGB), since technetium, having no stable isotopes, is a good diagnosis of the s-process of nucleosynthesis (Section 9); and (iii) pulsation mode from the location in the period–luminosity (*P*–$\mathcal{L}$) diagram (Section 10).

The results and graphical outputs presented in the paper were obtained using the modular software suite SPIDAST,[1] created to calibrate and interpret SPI measurements, particularly those obtained with VLTI/AMBER (Cruzalèbes, Spang & Sacuto 2008; Cruzalèbes et al. 2010, 2013a).

Throughout the present paper, uncertainties are reported using the concise notation, according to the recommendation of the Joint Committee for Guides in Metrology (JCGM-WG1 2008). The number between parentheses is the numerical value of the standard uncertainty referred to the associated last digits of the quoted result.

2 INTRODUCING THE OBSERVATIONS

2.1 Selecting the science targets for the programme

The sample contains supergiants and long-period variables, bright enough ($m_K < 2$) to be measured by the VLTI subarray [1.80 m aux-

iliary telescopes (ATs)] with high SNR. In Table 1, we compile their relevant observational parameters, including possible multiplicity and variability. On one hand, the scientific targets must be resolved well enough, which results in visibilities clearly smaller than unity. On the other hand, visibilities higher than ∼0.1 (*H* band) are necessary to allow the fringe-tracker FINITO[2] to work under optimal conditions (Gai et al. 2004). These two contradictory constraints impose the usable range of the spatial frequencies $f = B/\lambda$, where *B* is the baseline length and λ the observation wavelength, to be that associated with the second lobe of the uniform-disc (UD) visibility function. In the following, we use the term *resolution criterion* to summarize these constraints. They require that the maximum value of the dimensionless parameter $z = \pi\phi f$, where ϕ is the angular diameter, remains between 3.832, where the first zero of the UD visibility function appears, and 7.016 (second zero). For instance, observations in the *K* band with AMBER of scientific targets with angular diameters of 10 mas impose to the longest VLTI baseline length to be between 55 and 101 m (first and second zero). The choice of the *K* band is driven by the presence of the strong CO first-overtone transition around 2.33 μm, allowing to probe different layers in the photosphere within the same filter.

To increase the confidence in the measurements, we record multiple observations of each target per observing night. This observing procedure ensures obtaining sufficient amount of data to compensate for the fringe-tracking deficiency, occurring when the contrast is low or under poor-seeing conditions.

According to our resolution criterion, we select the scientific targets from two catalogues: CHARM2 (Richichi, Percheron & Khristoforova 2005) and CADARS (Pasinetti Fracassini et al. 2001), which compile angular diameter values derived from various methods. In order to observe them with similar instrumental configurations, we choose stars with approximately the same angular diameter (∼10 mas). The suitable calibrators are given in Table 1. Since the angular diameter of some of them is not found in the calibrator catalogues, we had to derive it from the fit of MARCS + TURBOSPECTRUM synthetic spectra on spectrophotometric measurements (Cruzalèbes et al. 2010, 2013a). For reasons of homogeneity, we applied this procedure to all calibrators.

2.2 Observation logbook

A sample of 16 cool stars – 10 O-rich giants, two supergiants and four C-rich giants – were observed in 2009 May (three nights), 2009 August (two nights), 2009 November (three nights), 2010 March (three nights) and 2010 December (four nights), using the AMBER instrument at the focus of ESO/VLTI, with three ATs. All observations were done using the medium-resolution-*K*-band spectral configuration, centred on λ = 2.3 μm, providing about 500 spectral channels with $\mathcal{R} = 1500$. The observation logbook is given in Cruzalèbes et al. (2013b).

3 DERIVING THE ANGULAR DIAMETERS

The true (calibrated) observables, defined hereafter, are derived from the AMBER output measurements, using the SPIDAST modular software suite we started to develop in 2006 (Cruzalèbes et al. 2008, 2010, 2013a). Recently made available to the community,[3] SPIDAST performs the following automatized operations: weighting

---

[1] Acronym for 'SPectro-Interferometric Data Analysis Software Tool'.

[2] Acronym for 'Fringe-tracking Instrument of NIce and TOrino'.

[3] https://forge.oca.eu/trac/spidast

Table 1. Relevant observational parameters of the observed sample of science targets.

Name	Spectral type[a]	ϖ_{Hip}[a] (mas)	m_K[b]	m_V[c]	A_V[d]	$(V-K)_0$	Component[e]	Separation[e] (arcsec)	Position angle[e] (°)	ΔV[e]	Variable type[c]	Period[c] (d)	Tc[g]	Calib[h]
α Car	F0II[8]	10.6(6)	−1.3(3)	−0.62(5)	0.07(15)	0.6(3)	–	–	–	–	–	–	unkn.	η Col
β Cet	K0III[13]	33.9(4)	−0.3(4)	1.96–2.11	0.03(19)	2.3(4)	–	–	–	–	SRB[17]	37(4)[17]	unkn.	η Cet
α TrA	K2II[14]	8.4(2)	−1.2(1)	1.91(5)	0.08(15)	3.1(2)	–	–	–	–	–	–	unkn.	ε TrA
α Hya	K3II–III[2]	18.1(2)	−1.1(2)	1.93–2.01	0.03(14)	3.1(3)	AB / AC	283 / 210	153 / 90	8	Susp.	–	unkn.	λ Hya
ζ Ara	K3III[3]	6.7(2)	−0.6(2)	3.12(5)	0.07(15)	3.7(3)	–	–	–	–	–	–	unkn.	ε TrA/o Sgr
δ Oph	M0.5III[2]	19.1(2)	−1.2(2)	2.72–2.75	0.03(15)	3.9(3)	AB	66	294	9	Susp.	–	unkn.	γ Lib/ε TrA
γ Hyi	M2III[1]	15.2(1)	−1.0(4)	3.32–3.38	0.04(16)	4.2(5)	–	–	–	–	SRB	–	unkn.	α Ret
o_1 Ori	M3III[5]	5.0(7)	−0.7(2)	4.65–4.88	0.16(17)	5.2(2)	AB[7]	–	–	11.7	SRB	30(1)	yes[6,11]	HR 2411
σ Lib	M3.5III[4]	11.3(3)	−1.4(2)	3.20–3.46	0.03(14)	4.6(3)	–	–	–	–	SRB	20(1)	no[6,11]	51 Hya/ε TrA
γ Ret	M4III[3]	7.0(1)	−0.5(3)	4.42–4.64	0.08(15)	4.9(4)	AB	0.2	–	–	SR	25(1)	unkn.	α Ret
CE Tau	M2Iab-b[3]	1.8(3)	−0.9(2)	4.23–4.54	0.29(19)	5.0(3)	–	–	–	–	SRC	165(1)	doubt.[6]	ϕ_2 Ori
T Cet	M5.5Ib/II[8]	3.7(5)	−0.8(3)	4.96–6.9	0.08(19)	6.4(3)	–	–	–	–	SRC	159.3(1)[9]	prob.[6]	ι Eri/γ Scl
TX Psc	C7,2(N0)(Tc)[10]	3.6(4)	−0.5(3)	4.79–5.20	0.11(10)	5.4(3)	–	–	–	–	LB	220(1)[9]	yes[6,16]	θ Psc
W Ori	C5,4(N5)[10]	2.6(10)[15]	−0.5(4)	5.5–6.9	0.11(15)	6.4(5)	–	–	–	–	SRB	212(1)	no[12,16]	ϕ_2 Ori/HR 2113
R Scl	C6,5ea(Np)[10]	2.1(15)[15]	−0.1(1)	9.1–12.9	0.11(10)	6.6(2)	AB[f]	10	234	12	SRB	370(1)	unkn.	ι Eri
TW Oph	C5,5(Nb)[10]	3.7(12)[15]	0.5(4)	11.6–13.8	0.10(16)	7.0(4)	–	–	–	–	SRB	185(1)	unkn.	o Sgr/γ Lib

[1]Landi Dessy & Keenan (1966); [2]Morgan & Keenan (1973); [3]Houk & Cowley (1975); [4]Houk (1978); [5]Smith & Lambert (1985); [6]Little, Little-Marenin & Bauer (1987); [7]Ake & Johnson (1988); [8]Houk & Smith-Moore (1988); [9]Wasatonic (1997); [10]Kholopov et al. (1998); [11]Lebzelter & Hron (1999); [12]Abia et al. (2001); [13]Montes et al. (2001); [14]Bordé et al. (2002); [15]Knapp et al. (2003); [16]Lebzelter & Hron (2003); [17]Otero & Moon (2006).

[a]Unless quoted, from the New HIPPARCOS Astrometric Catalogue (van Leeuwen 2007).
[b]From the 2MASS Catalogue (Skrutskie et al. 2006).
[c]Magnitude variations, variability type and period of variability taken (unless quoted) from the AAVSO-VSX Database (Watson et al. 2006). 'Susp.' stands for suspected variability.
[d]Calculated, thanks the numerical algorithm of Hakkila et al. (1997), including the studies of Fitzgerald (1968), Neckel & Klare (1980), Berdnikov & Pavlovskaya (1991), Arenou, Grenon & Gomez (1992), Chen et al. (1998) and Drimmel & Spergel (2001), plus a sample of studies of high-galactic-latitude clouds.
[e]Multiplicity parameters from the WDS Catalogue (Mason et al. 2001).
[f]The A component is seen twice by Maercker et al. (2012) with ALMA.
[g]Qualitative information on the technetium content (unkn. stands for 'unknown', doubt. for 'doubtful' and prob. for 'probable').
[h]Associated calibrator(s), with the angular diameter given by Cruzalèbes et al. (2013a).

of non-aberrant visibility and triple product data, fine spectral calibration at subpixel level, accurate and robust determination of stellar diameters for calibrator sources, and of their uncertainties as well, correction for the degradations of the interferometer response in visibility and triple product, fitting of parametric chromatic models on SPI observables, and extraction of model parameters.

We measure the angular diameter for each scientific target, by fitting synthetic limb-darkened brightness profiles on the visibility and the triple product. In an attempt to reproduce the behaviour of the true observables, especially in the second lobe of the visibility function, we use the numerical centre-to-limb variation (CLV) profile with respect to the impact parameter, given by the MARCS (Gustafsson et al. 2008) + TURBOSPECTRUM codes (Alvarez & Plez 1998; Plez 2012).

3.1 Computing reliable uncertainties

For each observing block (OB), the angular diameter is given by the modified gradient-expansion algorithm (Bevington & Robinson 1992), a robust fitting technique based on the minimization of the weighted χ^2, and adapted from Marquardt (1963). As 'robust', we mean a final result insensitive to small departures from the model assumptions from which the estimator is optimized (Huber & Ronchetti 2009). We improve the robustness of the results of the fitting process by removing input measurements with low SNR (< 3), as well as values considered as extremal residuals, i.e. showing exceedingly large discrepancies with the model.

Since the data used for the fit are obtained from a complex cross-calibration process, we cannot ensure that the final uncertainties follow a normal distribution, but the χ^2 function remains usable as the merit function for finding the best-fitting model parameters. However, the formal output-parameter uncertainties, deduced from the diagonal terms of the covariance matrix of the best-fitting parameters, give irrelevant and usually underestimated values (Press et al. 2007; Enders 2010). In our study, we deduce reliable uncertainties from the boundaries of the 68 per cent confidence interval of the residual-bootstrap distribution of the best-fitting angular diameters (Efron 1979, 1982; Cruzalèbes et al. 2010).

3.2 Choosing the model input parameters

Table 2 lists the stellar parameters of the science targets: effective temperature, surface gravity, and mass, of the MARCS models

Table 2. Fundamental parameters used as entries in the MARCS models.

| Target(s)	T_{eff} (K)	$\log g$	$\mathcal{M}/\mathcal{M}_\odot$	[Fe/H]	[α/Fe]	C/O
α Car	7000	2.0	5.0	0.0	0.0	0.54
β Cet	4660	2.1	1.0	0.0	0.0	0.54
α TrA	4350	1.15	2.8	0.0	0.0	0.54
α Hya	4300	1.3	1.1	0.0	0.0	0.54
ζ Ara	4250	1.9	1.8	-0.5	0.2	0.54
δ Oph	3650	1.3	1.2	0.25	0.0	0.54
γ Hyi	3500	1.0	1.0	0.0	0.0	0.54
o_1 Ori	3450	0.8	0.9	0.0	0.0	0.54
σ Lib	3450	0.8	0.9	0.0	0.0	0.54
γ Ret	3450	0.8	0.9	0.0	0.0	0.54
CE Tau	3400	0.0	12.0	0.0	0.0	0.54
T Cet	3250	-0.5	7.0	0.0	0.0	0.54
TX Psc	3000	0.0	2.0	-0.5	0.2	1.02
R Scl	2600	0.0	2.0	0.0	0.0	1.35
W Ori	2600	0.0	2.0	0.0	0.0	1.17
TW Oph	2600	0.0	2.0	0.0	0.0	1.17
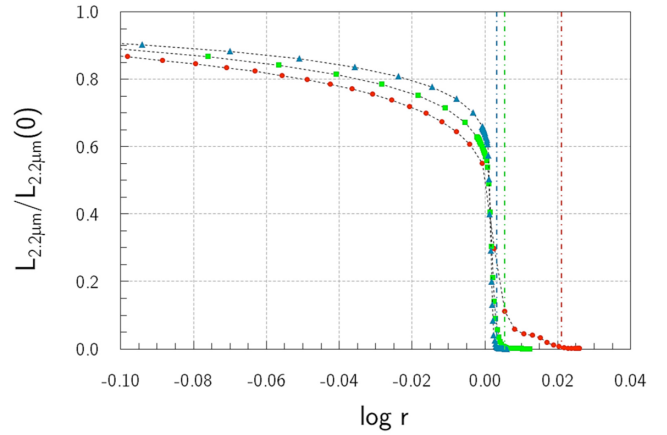
Figure 1. Model CLV profiles at $\lambda = 2.2\,\mu$m for: β Cet (blue triangles); δ Oph (green squares); and TX Psc (red circles). The dot–dashed vertical lines show the values of the impact parameter at 0.5 per cent of the intensity: 1.008 for β Cet, 1.013 for δ Oph and 1.050 for TX Psc (r is in units of the Rosseland radius).

used in the regression process, with the microturbulence parameter $\xi_{turb} = 2$ km s^{-1}. We derive these parameters from the two-dimensional B-spline interpolation of the tables of $\log T_{eff}$ (de Jager & Nieuwenhuijzen 1987), $\log g$ (Allen 2001) and $\mathcal{L}/\mathcal{L}_\odot$ (Allen 2001), with respect to the spectral type.

Because this method relies on the spectral type, which carries some level of subjectivity, we concede that it is probably not the most accurate method for the determination of fundamental stellar parameters (see also the discussion in relation with Fig. 5 in Section 8). However, this method, currently used to measure the angular diameters of interferometric calibrators (Bordé et al. 2002; Cruzalèbes et al. 2010), provides a homogeneous way to convert various spectral types into fundamental parameters, all over the HRD. In Section 4, we investigate the sensitivity of the angular diameters to the adopted model stellar parameters, and show that this sensitivity is not an issue.

3.3 Fitting the model limb-darkened intensity

The spherically symmetric MARCS model atmospheres, assuming local thermodynamic and hydrostatic equilibrium, are characterized by the following parameters: effective temperature T_{eff}, surface gravity g, and mass $\mathcal{M}$, with $g = G\mathcal{M}/\mathcal{R}_{Ross}^2$, where $\mathcal{R}_{Ross}$ is the radius at $\tau_{Ross} = 1$. Using the TURBOSPECTRUM code,[4] we compute CLVs of the monochromatic radial intensity $L_\lambda(r)$ (also called *spectral radiance*, in W m^{-2} μm^{-1} sr^{-1}), where $r = \mathcal{R}/\mathcal{R}_{Ross}$ is the impact parameter. Fig. 1 shows the CLV profiles, at $\lambda = 2.2\,\mu$m, calculated with TURBOSPECTRUM using a MARCS model, with three different sets of input parameters (Table 2), associated with: β Cet (O-rich star, blue triangles); δ Oph (O-rich star, green squares); and TX Psc (C-rich star, red circles).

According to the Van Cittert–Zernike theorem (Goodman 1985), the monochromatic synthetic visibility of a centro-symmetric brightness distribution of the angular diameter ϕ is

$$V_\lambda(\phi) = 2\pi \frac{\left| \int_0^{r_{out}} L_\lambda(r)\ J_0\left(\pi r\phi\frac{B}{\lambda}\right)\ r\,\mathrm{d}r \right|}{M_\lambda}, \tag{1}$$

---

[4] In the K band, we include all isotopomers of CO, C2, CN as well as H$_2$O^{16}, and the atomic lists extracted from Uppsala-VALD.
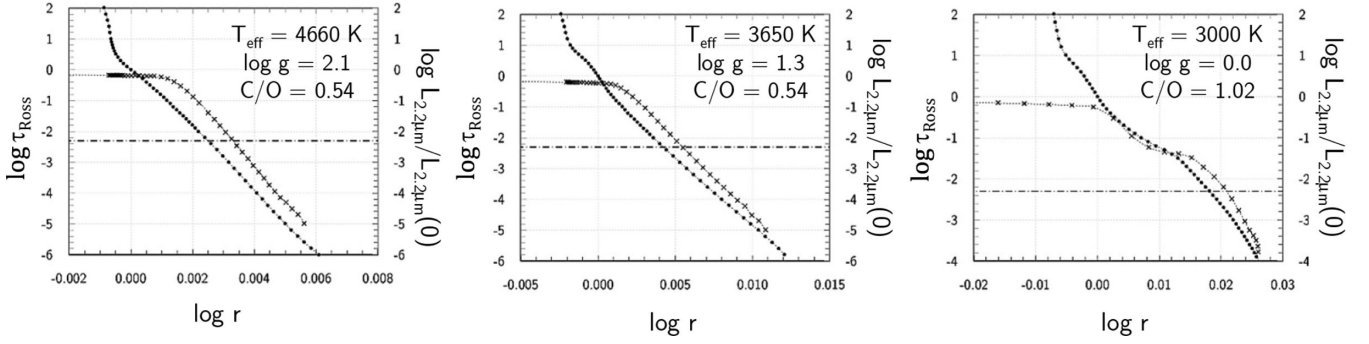
Figure 2. Rosseland optical depth (dots, left-hand axis) and CLV profile at $\lambda = 2.2\,\mu m$ (crosses, right-hand axis) with respect to the impact parameter (in units of the Rosseland radius) for different MARCS models (left-hand and central panels: O-rich stars; right-hand panel: C-rich stars). The dot–dashed horizontal lines: limit of instrumental sensitivity (0.5 per cent).

where J_0 is the Bessel function of the first kind of order 0, r_{out} is the dimensionless parameter defined as $r_{out} = \mathcal{R}_{out}/\mathcal{R}_{Ross}$, where $\mathcal{R}_{out}$ is the outer radius, and $M_\lambda = 2\pi \int_0^{r_{out}} L_\lambda(r)\, r\, dr$ is the monochromatic flux (also called *spectral radiant exitance*, in W m^{-2} μm^{-1}). Numerical integration from 0 to r_{out} is performed using the trapezoidal rule on a grid, with a step width decreasing from the centre to the limb.

To be accurately evaluated, the integral on r in equation (1) requires $L_\lambda(r)$ to be extended all the way to a value of r_{out} corresponding to the lower boundary of the sensitivity of the AMBER instrument. In the K band, this boundary has been measured around 0.5 per cent of the maximum emission (Absil et al. 2010; Duvert et al. 2010). With the MARCS models, the lower boundaries of the Rosseland optical depth, used to compute the intensity distributions $L_\lambda(r)$, are $\tau_{Ross} = 10^{-6}$ for O-rich stars, and $\tau_{Ross} = 10^{-4}$ for C-rich stars (Fig. 2). Thus, $\mathcal{R}_{out} = \mathcal{R}\left(\tau_{Ross} = 10^{-6}\right)$ for O-rich stars, and $\mathcal{R}_{out} = \mathcal{R}\left(\tau_{Ross} = 10^{-4}\right)$ for C-rich stars. These bottom levels ensure that the blanketing is correctly taken into account, and that the thermal structure in the line-forming region remains unchanged with respect to atmospheres that would be computed with even smaller optical-depth boundaries. According to Fig. 2, these optical-depth lower boundaries are associated with intensity levels of $<10^{-5}$ and $\sim 10^{-4}$, respectively, thus far below the instrumental sensitivity, as it should be to work in safe conditions. Moreover, in Section 4, we evaluate the sensitivity of the angular diameter to the MARCS model used to compute the CLV.

Fig. 3 shows three typical results of the MARCS-CLV fits obtained with the visibility measurements of individual OBs, for β Cet, δ Oph and TX Psc. For the sake of clarity, the true visibility values are shown without error bars. In addition to the fit of the MARCS-CLV profile on the true visibilities, we also compute the angular diameter using fits on triple product data (Table 4).

4 STUDYING THE SENSITIVITY TO MODEL PARAMETERS

The effective temperature, surface gravity and stellar mass adopted for the MARCS model representing a given star are derived from the spectral type (Section 3.2). Unfortunately, neither the gravity nor the stellar mass is strongly constrained by the spectral type alone. Therefore, there is a disagreement between the MARCS-model parameters and the true stellar values. In this section, we study for the two targets ζ Ara (K giant) and TX Psc (carbon star) the sensitivity of the angular diameter to a change of input parameter values such as T_{eff}, $\log g$ and ξ_{turb}.

Table 3 shows the sensitivity to the model parameters of the angular diameter, deduced from the fit on visibility data. The top part of the table is for ζ Ara observed at MJD = 549 75.36 and the bottom part is for TX Psc observed at MJD = 551 43.10. The uncertainties in angular diameter are the formal 1σ fitting errors. The choice of the different values of T_{eff} and $\log g$ used for this analysis is based on the typical uncertainties, 300 K and 1 dex respectively, the latter coming from the *a posteriori* determination of the gravity (Section 8 and Fig. 7). The sensitivity to ξ_{turb} is studied with the values 2 and 5 km s^{-1}, for the carbon star.

The highest deviations from the nominal values of the angular diameter, i.e. 0.03 mas for ζ Ara and 0.07 mas for TX Psc, are smaller than the final uncertainties, 0.12 and 0.36 mas, respectively (Table 4). Although we cannot infer quantitative general sensitivity rules from only two examples, our results show that such changes as 300 K for T_{eff}, roughly 1 dex for $\log g$ and a factor of 2 for ξ_{turb} induce variations on the final angular diameter which are smaller than its absolute uncertainty.

5 STUDYING THE TEMPORAL VARIABILITY OF THE ANGULAR DIAMETER

To study the temporal variability of the angular diameter, we group together the observing blocks of the same observing epoch over consecutive days, for each scientific target. Table 4 gives the best-fitting angular diameters of the scientific targets, separately for each observation epoch and for the average over all runs. MJD is the Modified Julian Day for the middle of each observing period. The notations ϕ_V and $\phi_{\mathscr{T}}$ stand for the weighted means of the angular diameters resulting from fits of the MARCS CLVs on visibility and triple product data, respectively.

Fig. 4 shows the temporal behaviour of the best-fitting angular diameter, for our scientific targets observed over different epochs. Except for TX Psc, which shows two different values of ϕ_V, but not of $\phi_{\mathscr{T}}$, we find no evidence for temporal variation of the angular diameter for our targets, given the uncertainties. To perform a meaningful study of the angular diameter time variability, a larger amount of data would have been needed for our targets. Unfortunately, we did not succeed in convincing the Observing Programmes Committee to allow supplementary observing time for this purpose.

6 COMPUTING THE FINAL ANGULAR DIAMETER

Rather than applying a global fit on all data sets (see e.g. Le Bouquin et al. 2008; Domiciano de Souza et al. 2008), which is the commonly
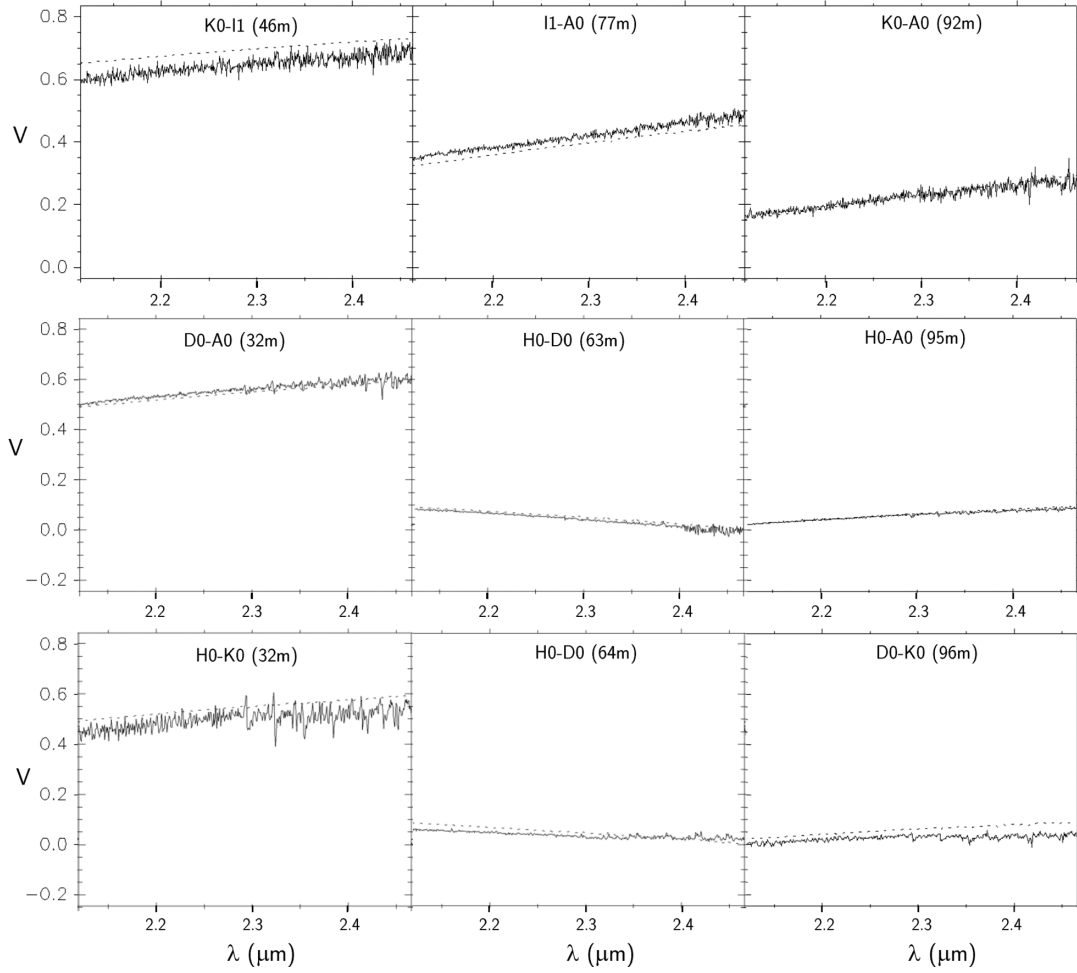
Figure 3. Three examples of MARCS-CLV fitting results, obtained with visibility measurements: β Cet in the top panels (MJD = 554 43.16); δ Oph in the middle panels (MJD = 549 75.24); and TX Psc in the bottom panels (MJD = 551 43.07). The baselines are projected on the sky. The model visibility profiles at medium spectral resolution ($\mathscr{R} = 1500$) are in short dashes. The measured median absolute uncertainties in visibility are (from the left-hand to right-hand side): for β Cet: 0.02, 0.03 and 0.02; for δ Oph: 0.010, 0.004 and 0.003; and for TX Psc: 0.015, 0.003 and 0.004.

Table 3. Sensitivity of the angular diameter ϕ (in mas) with respect to the model parameters (gravities are in cgs units).

	T_{eff} (K)	$\log g = 1.05$	$\log g = 1.9$
ζ Ara	3950	$\begin{cases} \phi = 7.060(2) \\ \chi^2 = 2.03 \end{cases}$	$\begin{cases} \phi = 7.083(2) \\ \chi^2 = 1.98 \end{cases}$
	4250	$\begin{cases} \phi = 7.039(2) \\ \chi^2 = 2.01 \end{cases}$	$\begin{cases} \phi = 7.066(1) \\ \chi^2 = 1.83 \end{cases}$
	T_{eff} (K)	$\xi_{\text{turb}} = 2 \text{ km s}^{-1}$	$\xi_{\text{turb}} = 5 \text{ km s}^{-1}$
TX Psc	3000	$\begin{cases} \phi = 10.053(2) \\ \chi^2 = 21.5 \end{cases}$	$\begin{cases} \phi = 9.986(2) \\ \chi^2 = 22.5 \end{cases}$

used method with VLTI/AMBER data, we propose to combine multiple measurements obtained for a given star under different instrumental and environmental circumstances (see e.g. Ridgway et al. 1980; Richichi et al. 1992; Dyck et al. 1996). Using the visibility and the triple product, we compute the angular diameter averaged over all OBs, with a weighting factor derived from the uncertainty on the angular diameter, the quality of the fit and the seeing conditions during each OB. Then, we combine the two angular diameter

values, which leads to a unique final value (last column of Table 4). We note that δ Oph is the only star for which ϕ_V and $\phi_{\mathscr{T}}$ are significantly different (up to 10 per cent, as seen in Table 4 and Fig. 4), although we have no explanation for that discrepancy.

7 CONFRONTING OUR RESULTS WITH THOSE OF THE LITERATURE

Here, we compare our final angular diameter values with those derived from measurements obtained by other instruments or methods. Table 5 gathers the values published in the literature, related to limb-darkened models, derived from indirect methods: lunar occultation (LO) and long-baseline interferometry (LBI). These values are obtained in various spectral ranges and related to various photospheric models. Their large dispersions make them difficult to use in a direct comparison with our results, which are repeated in the ϕ_{LBI} column under Reference (48). Therefore, we believe that the only meaningful comparison is between our values and those from the literature obtained with LBI in the same spectral domain (K band), as done in the last column of Table 5.

Apart for TX Psc, only small differences are found between our new values and the published LBI values for the seven science targets α Car, β Cet, α Hya, δ Oph, CE Tau, W Ori and R Scl. Such

Table 4. Best-fitting angular diameters derived from the visibility and the triple product, for each observation epoch, and final angular diameters of the science targets, after averaging over all OBs. MJD is the Modified Julian Day for the middle of each observation period.

Name	MJD (d)	ϕ_V (mas)	$\phi_{\mathscr{T}}$ (mas)	ϕ_{final} (mas)
α Car	54 143.26	6.78(45)	6.64(1)	6.92(11)
	55 269.14	6.78(17)	6.93(2)	
β Cet	55 541.17	5.84(40)	5.45(5)	5.51(25)
α TrA	54 976.23	9.23(10)	9.26(8)	9.24(2)
	55 052.12	8.85(18)	9.05(5)	
	55 269.32	9.34(2)	9.34(3)	
α Hya	55 269.23	9.37(5)	9.35(7)	9.36(6)
ζ Ara	54 976.25	7.10(5)	7.09(13)	7.09(12)
	55 053.18	6.86(11)	6.98(13)	
δ Oph	54 976.22	10.05(4)	9.46(7)	9.93(9)
	55 051.99	10.02(2)	9.34(2)	
	55 269.88	10.43(21)	9.47(6)	
γ Hyi	55 539.80	8.77(6)	8.82(12)	8.79(9)
o_1 Ori	55 144.24	8.93(15)	10.04(5)	9.78(10)
σ Lib	55 268.81	11.73(14)	11.19(3)	11.33(10)
γ Ret	55 539.83	7.44(2)	7.44(2)	7.44(2)
CE Tau	55 143.28	9.94(7)	10.07(2)	9.97(8)
	55 541.24	9.94(7)	10.04(12)	
T Cet	55 143.13	9.60(11)	9.70(1)	9.70(8)
TX Psc	55 143.08	9.61(21)	10.04(2)	10.23(36)
	55 541.07	10.60(6)	10.02(45)	
W Ori	55 143.72	9.62(1)	9.79(7)	9.63(4)
R Scl	55 143.56	10.31(5)	9.88(2)	10.06(5)
TW Oph	54 976.35	10.59(38)	9.53(20)	9.46(30)
	55 052.19	9.19(35)	9.71(21)	

a good agreement supports the validity and the reliability of our method, which gives, in addition, reliable uncertainties. Our study provides the first LBI determinations of the angular diameter for eight other targets: α TrA, ζ Ara, γ Hyi, o_1 Ori, σ Lib, γ Ret, T Cet and TW Oph.

Coming back to TX Psc, this star has often been observed in the past using high-resolution techniques, giving an angular diameter slightly larger than our new measurement. Given the error bars, our value is in good agreement with the value from Barnes, Evans & Moffett (1978), derived from the visual surface brightness method. Richichi et al. (1995) attribute to the temporal variability of ϕ already noted previously for TX Psc (an Lb-type variable) most of the disagreement between their LO measurement and the LBI values of Quirrenbach et al. (1994), obtained in the red part of the visible spectral domain with the MkIII Optical Interferometer, and of Dyck, van Belle & Benson (1996), obtained at 2.2 μm with the IOTA interferometer. From repeated measurements, Quirrenbach et al. suggested a substantial variation of the angular diameter, correlated with the visual magnitude, varying from 4.8 to 5.2 in 220 days (Watson, Henden & Price 2006). As shown in Section 5, our data tend to confirm this variation.

8 HERTZSPRUNG–RUSSELL DIAGRAM

In this section, we use the values of the angular diameters of our calibrators and science targets to infer their location in the HRD (T_{eff}–$\mathcal{L}$).

The luminosity $\mathcal{L}$ is defined, in the MARCS models, from the relation $\mathcal{L} = 4\pi\mathcal{R}_{\text{Ross}}^2 F(\mathcal{R}_{\text{Ross}})$, where $F(\mathcal{R}_{\text{Ross}})$ is the flux per unit surface emitted by the layer located at the Rosseland radius (Gustafsson et al. 2008). The effective temperature T_{eff} is then defined according to $F(\mathcal{R}_{\text{Ross}}) = \sigma T_{\text{eff}}^4$.

We convert the best-fitting angular diameter ϕ into an empirical Rosseland radius $\mathcal{R}_{\text{obs}}$, thanks to the parallax ϖ. For the calibrators, ϕ is given by the fit of the model spectrum on the flux data. For the science targets, ϕ is given by the fit of the CLV profile on the
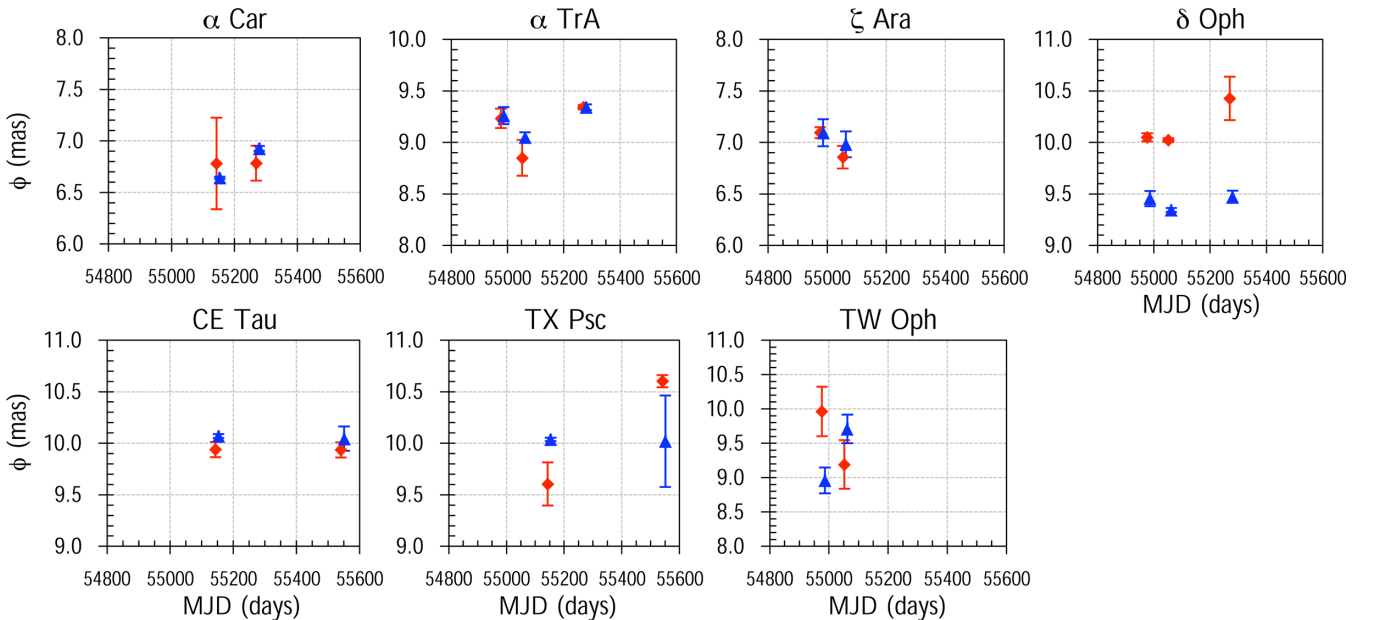

Figure 4. Temporal behaviour of the best-fitting angular diameter, from visibilities (red diamonds) and triple products (blue triangles). Top panels: science targets showing no photometric variation; bottom panels: targets known as photometric variables (i.e. with a GCVS entry). The symbols which mark the results associated with the same observing epoch are slightly shifted horizontally, in order to separate the error bars.

Table 5. Published angular diameters (in mas) of the scientific targets. We note ϕ_{ind} the angular diameter derived from indirect methods, while we note ϕ_{LO} and ϕ_{LBI} the limb-darkened angular diameters derived from LO and LBI measurements, respectively. The values in bold are the averaged values, using weights inversely proportional to the uncertainties. When not quoted, conservative 10 per cent errors are adopted. 'Reference' stands for the bibliographical reference from which each value is taken, as listed at the end of the table, and 'Difference' stands for the relative difference between our new measurement and the averaged published LBI values obtained with a similar instrumental configuration. Our values are included in the ϕ_{LBI} column under Ref. (48).

Name	ϕ_{ind}	Reference	ϕ_{LO}	Reference	ϕ_{LBI}	Reference	Difference
α Car	5.9(4)	16			6.6(8)	5	
	6.0(7)	3			6.86(41)	2	
	6.5(8)	11			6.92(11)	48	−0.1%
	6.8(4)	13			6.93(15)	42	
	7.1(2)	9					
	7.22(42)	37					
	6.7				**6.9**		
β Cet	5.03(40)	19			5.29(8)	46	
	5.31(6)	35			5.329(5)	44	
	5.4(8)	16			5.51(25)	48	+3.4%
	5.66(39)	45					
	6.5	24					
	7.4(9)	3					
	8.0	20					
	5.6				**5.3**		
α TrA	11.6(17)	16			9.24(2)	48	
	8.98(10)	35					
	9.81(39)	40					
	15.0(18)	3					
	9.5						
α Hya	9.30(39)	9			9.73(10)	38	
	9.4(9)	23			9.335(16)	44	
	9.9(10)	13			9.36(6)	48	+0.3%
	10.0(15)	16					
	14.0(17)	3					
	10.0				**9.4**		
ζ Ara	7.21(21)	39			7.09(12)	48	
	7.2	20					
	7.6(11)	16					
	7.62(53)	45					
	9.0	24					
	11.0(13)	3					
	7.6						
δ Oph	10(1)	21			9.50(50)	30	
	10.03(10)	35			9.93(9)	48	+2.1%
	10.18(20)	25			9.946(13)	44	
	10.22(71)	45			10.47(12)	38	
	10.23(31)	40					
	11.6(17)	16					
	11.0	24					
	13	1					
	13.0(16)	3					
	26(7)	8					
	10.4				**10.0**		
γ Hyi	9.5	33			8.79(9)	48	
	9.8(15)	16					
	10.0(12)	3					
	9.7						
o_1 Ori	7.1(21)	3			9.78(10)	48	
σ Lib	11.0(13)	3			11.33(10)	48	
	12.05(83)	45					
	12.5	20					
	13.0	24					
	12.1						

Table 5 – *continued*

Name	$\phi_{\rm ind}$	Reference	$\phi_{\rm LO}$	Reference	$\phi_{\rm LBI}$	Reference	Difference
γ Ret	7.5(2)	32			7.44(2)	48	
	8.0	33					
	11.0(33)	16					
	7.8						
CE Tau	9.4(11)	3	9.1(8)	15	9.3(5)	34	
	13	1	10.9(10)	14	9.83(7)	30	
	13.0(20)	16	17(1)	18	9.97(8)	48	+3.7%
					10.68(21)	27	
	11.5		**12.1**		**10.0**		
T Cet	13.1(39)	16			9.70(8)	48	
	14.5	43					
	14.1						
TX Psc	6.2	12	8.40(5)	29	10.23(36)	48	−10.6%
	9.5(5)	11	8.9(10)	4	11.2(10)	28	
			9.31(75)	10	11.44(30)	31	
			10(3)	6			
			10.2(25)	7			
	8.0		**8.5**		**10.9**		
W Ori					9.63(4)	48	−2.8%
					9.91(60)	31	
					9.7		
R Scl	12.2	22			10.06(5)	48	−1.4%
	12.0	26			10.2(5)	47	
	12.1	41					
	12.75(98)	36					
	12.3				**10.1**		
TW Oph			10.4(5)	17	9.46(30)	48	

(1) Hertzsprung (1922); (2) Hanbury Brown et al. (1967); (3) Wesselink, Paranya & DeVorkin (1972); (4) de Vegt (1974); (5) Hanbury Brown, Davis & Allen (1974); (6) Morbey & Fletcher (1974); (7) Dunham et al. (1975); (8) Currie et al. (1976); (9) Blackwell & Shallis (1977); (10) Ridgway, Wells & Joyce (1977); (11) Barnes et al. (1978); (12) Scargle & Strecker (1979); (13) Blackwell, Petford & Shallis (1980); (14) White (1980); (15) Beavers, Cadmus & Eitter (1982); (16) Ochsenbein & Halbwachs (1982); (17) Ridgway et al. (1982); (18) White, Kreidl & Goldberg (1982); (19) Eriksson, Linsky & Simon (1983); (20) Johnson & Wright (1983); (21) Leggett et al. (1986); (22) Rowan-Robinson et al. (1986); (23) Bell & Gustafsson (1989); (24) Slee et al. (1989); (25) Blackwell et al. (1990); (26) Judge & Stencel (1991); (27) Quirrenbach et al. (1993); (28) Quirrenbach et al. (1994); (29) Richichi et al. (1995); (30) Dyck et al. (1996); (31) Dyck et al. (1996); (32) Bedding et al. (1997); (33) Dumm & Schild (1998); (34) Dyck, van Belle & Thompson (1998); (35) Cohen et al. (1999); (36) Yudin & Evans (2002); (37) Decin et al. (2003); (38) Mozurkewich et al. (2003); (39) Ohnaka et al (2005); (40) Engelke, Price & Kraemer (2006); (41) Dehaes et al. (2007); (42) Domiciano de Souza et al. (2008); (43) Ramstedt, Schöier & Olofsson (2009); (44) Richichi, Percheron & Davis (2009); (45) Lafrasse et al. (2010); (46) Berio et al. (2011); (47) Sacuto et al. (2011); (48) present work.

SPI data. Thus, we compute the empirical luminosity $\mathcal{L}_{\rm obs}$ using the logarithmic formula

$$\log \frac{\mathcal{L}_{\rm obs}}{\mathcal{L}_\odot} \approx 4 \log T_{\rm eff} + 2 \log \frac{\phi}{\varpi} - 10.984(7), \qquad (2)$$

where $T_{\rm eff}$ is in K, using the solar values $T_{\rm eff,\,\odot} = 5777(10)$ K (Smalley 2005), and $\mathcal{R}_\odot = 0.004\,6492(2)$ au (Brown & Christensen-Dalsgaard 1998; Amsler et al. 2008).

Table 6 gives the final fundamental parameters of our science targets and calibrators. The uncertainty-propagation formulae given by Winzer (2000), based on the second-order Taylor approximation, are used to compute the uncertainties on the derived fundamental parameters. For input uncertainties larger than 30 per cent, we use the confidence interval transformation principle (see e.g. Smithson 2002; Kelley 2007).

To ensure consistency with the fitting process, which uses as model input parameters those derived from the spectral type

(Cruzalèbes et al. 2013a and Table 2), the value adopted for the effective temperature of the star is the value listed in Table 2.

To assess the accuracy of the value, we compare the effective temperature deduced from the spectral type for the giants and supergiants of types K and M, included in our samples of science and calibrator targets, with the temperature derived from the dereddened $V - K$ index, using the empirical relationship provided by van Belle et al. (1999):

$$T_{\rm eff}({\rm K}) = 3030 + 4750 \times 10^{-0.187(V-K)}, \qquad (3)$$

where $2 < V - K < 9$. We find that the agreement between the effective temperatures, shown in Fig. 5, is quite satisfactory, since their discrepancy is less than ± 300 K, which is of the same order as the absolute uncertainty given by van Belle's formula (± 250 K). For the three carbon stars W Ori, R Scl and TW Oph, the adopted effective temperature of 2600 K (Table 2) is consistent with the

Table 6. Final values of the stellar fundamental parameters (top part: science targets; bottom part: calibrators).

Name	$\mathcal{R}_{obs}/\mathcal{R}_{\odot}{}^a$	$\log T_{eff}{}^b$	$\log \mathcal{L}_{obs}/\mathcal{L}_{\odot}{}^c$	$M_{bol}{}^d$	$\mathcal{M}/\mathcal{M}_{\odot}{}^e$	$\log g_{obs}{}^f$	Q^g
α Car	71(4)	3.845(6)	4.03(5)	$-5.34(13)$	8.0(3)	1.64(5)	–
β Cet	17.5(9)	3.668(9)	2.21(6)	$-0.54(14)$	3.0(3)	2.43(6)	0.879(121)
α TrA	119(2)	3.638(10)	3.66(4)	$-4.41(11)$	7–8	1.16(3)	–
α Hya	55.7(7)	3.633(10)	2.98(4)	$-2.71(10)$	4–5	1.60(5)	–
ζ Ara	114(4)	3.628(10)	3.58(5)	$-4.21(12)$	7–8	1.20(4)	–
δ Oph	56.0(7)	3.562(12)	2.70(5)	$-2.01(12)$	1.0(3)	0.93(12)	–
γ Hyi	62(1)	3.544(12)	2.71(5)	$-2.05(13)$	1.0(3)	0.84(12)	–
o_1 Ori	214(29)	3.538(13)	3.76(13)	$-4.65(31)$	3–4	0.32(13)	0.019(4)
σ Lib	108(3)	3.538(13)	3.17(5)	$-3.18(14)$	1.5–2	0.61(7)	0.024(2)
γ Ret	115(2)	3.538(13)	3.23(5)	$-3.33(13)$	1.5–2	0.55(6)	0.027(2)
CE Tau	601(83)	3.531(13)	4.63(13)	$-6.83(32)$	8.0(3)	$-0.21(12)$	0.033(7)
T Cet	275(34)	3.531(13)	3.91(12)	$-5.03(30)$	3.0(3)	0.01(11)	0.059(11)
TX Psc	293(66)	3.512(13)	$3.90\binom{21}{31}$	$-5.02(61)$	1.8(3)	$-0.30(21)$	0.056(17)
W Ori	406(185)	3.415(17)	$3.83\binom{51}{37}$	$-4.85(103)$	1–2	$-0.60\binom{42}{63}$	$0.032\binom{30}{20}$
R Scl	513(721)	3.415(17)	$4.04\binom{117}{55}$	$-5.35(201)$	2–3	$-0.59(75)$	$0.050\binom{76}{44}$
TW Oph	278(102)	3.415(17)	$3.50\binom{42}{34}$	$-4.02(89)$	1.0(3)	$-0.46\binom{38}{47}$	$0.040\binom{32}{21}$
α Ret	13.5(3)	3.679(9)	1.93(4)	$-0.10(11)$	2.5–3	2.61(5)	–
φ_2 Ori	8.8(1)	3.669(9)	1.52(4)	0.95(10)	1–2	$2.73\binom{13}{19}$	–
η Col	37.1(12)	3.668(9)	2.77(5)	$-2.17(12)$	5.0(3)	2.00(4)	–
λ Hya	9.7(8)	3.668(9)	1.60(8)	0.74(20)	1–2	$2.64\binom{20}{25}$	–
γ Lib	12.4(6)	3.668(9)	1.81(6)	0.21(14)	2.0(3)	2.55(7)	–
o Sgr	11.7(9)	3.668(9)	1.76(7)	0.33(19)	2.0(3)	2.60(8)	–
ι Eri	11.7(10)	3.663(9)	1.74(8)	0.40(21)	1–2	$2.48\binom{20}{25}$	–
θ Psc	10.4(7)	3.662(9)	1.63(7)	0.67(17)	1–1.5	2.50(14)	–
γ Scl	12.3(1)	3.654(10)	1.75(4)	0.37(10)	1–1.5	2.35(10)	–
HR 2113	35(4)	3.647(10)	2.62(10)	$-1.82(24)$	3–4	1.90(11)	–
ε TrA	16.2(2)	3.647(10)	1.96(4)	$-0.16(10)$	1–2	$2.20\binom{14}{19}$	–
η Cet	13.6(1)	3.647(10)	1.81(4)	0.22(10)	1–1.5	2.26(9)	–
HR 3282	78(6)	3.636(10)	3.28(8)	$-3.45(20)$	6–7	1.47(8)	–
HR 2411	22.7(10)	3.629(10)	2.18(6)	$-0.72(14)$	1–2	$1.90\binom{16}{21}$	–
51 Hya	11.6(6)	3.629(10)	1.60(6)	0.74(16)	1.0(3)	2.30(12)	–

^{a}Rosseland radius derived from the angular diameter ϕ and the parallax ϖ.
^{b}Effective temperature of the model (in K).
^{c}Empirical stellar luminosity, derived from equation (2).
^{d}Bolometric magnitude derived from the stellar luminosity.
^{e}Stellar mass derived from the position along the evolutionary track in the HRD. If two tracks with different masses pass through the star location, two possible mass values are listed.
^{f}Surface gravity, derived from equation (4).
^{g}Pulsation constant (in days), derived from equation (5).

values derived by Lambert et al. (1986) with ± 100 K uncertainty: respectively, 2680 , 2550 and 2450 K.

Fig. 6 shows the resulting T_{eff}–$\mathcal{L}_{obs}$ diagram, including the calibrators and the science targets. In order to distinguish between the error bars, the data points for R Scl, W Ori and TW Oph are slightly shifted horizontally, although these three carbon stars have the same effective temperature 2600 K. This HRD displays as well evolutionary tracks from the Padova set (Bertelli et al. 2008, 2009), for $Y = 0.26$ and $Z = 0.017$, and for masses between 1 and 8 $\mathcal{M}_{\odot}$, where Y is the helium abundance and Z the metallicity.

These tracks make it possible to derive a rough estimate of the stellar mass $\mathcal{M}$, thus of the gravity g_{obs} at the Rosseland surface, deduced from the relation

$$\log g_{obs} \approx \log \frac{\mathcal{M}}{\mathcal{M}_{\odot}} - 2 \log \frac{\mathcal{R}_{obs}}{\mathcal{R}_{\odot}} + 4.4374(5), \qquad (4)$$

using the value of the solar surface gravity given by Gray (2005). These mass and gravity values are also included in Table 6. The comparison of the surface gravities $\log g$, deduced from the spectral

type and used to select the MARCS models, with those derived *a posteriori* from the HRD, is done in Fig. 7. We see that they agree within ± 0.5 dex, except for the calibrator α Ret ($\log g - \log g_{obs} = -0.80$), and for the science targets α Car ($+0.82$) and ζ Ara ($+0.67$). Since the determination of the mass from the position along the evolutionary tracks in the HRD is well constrained,[5] we attribute the discrepancy in surface gravity to the ill-defined value derived from the spectral type and used for the model, at least for these three targets.

With the linear radius derived from the interferometry, and the luminosity following the relationship $\mathcal{L} = 4\pi \mathcal{R}^2 \sigma T_{eff}^4$, the location of our targets in the HRD allows us to perform interesting checks of stellar structure related to the presence or absence of technetium, and to the period–luminosity relationship.

[5] We note, however, that the mass inferred from the HRD tracks corresponds to the *initial* mass. However, substantial mass loss along the evolution may significantly reduce the current mass below its initial value, implying that g_{obs}, as we derive it, could be somewhat overestimated.
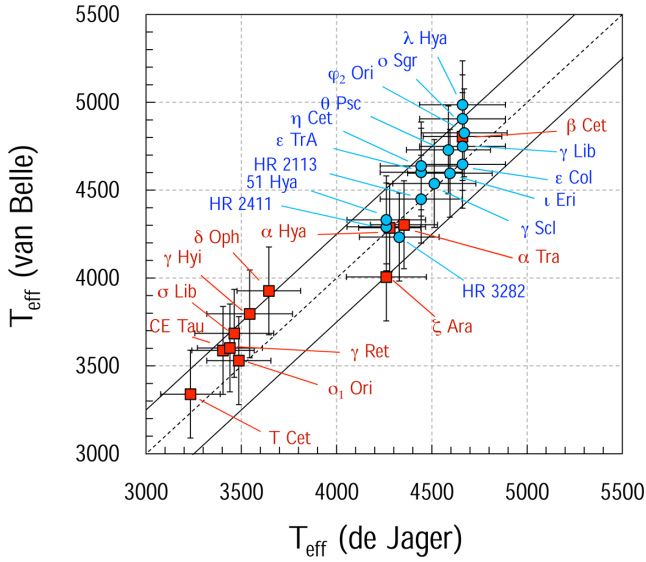
Figure 5. Effective temperatures deduced from the dereddened $V - K$ colour index (van Belle), versus from the spectral type (de Jager), for the targets of our observing sample. Red squares: science targets. Blue dots: calibrators. Solid lines: ±250 K thresholds.
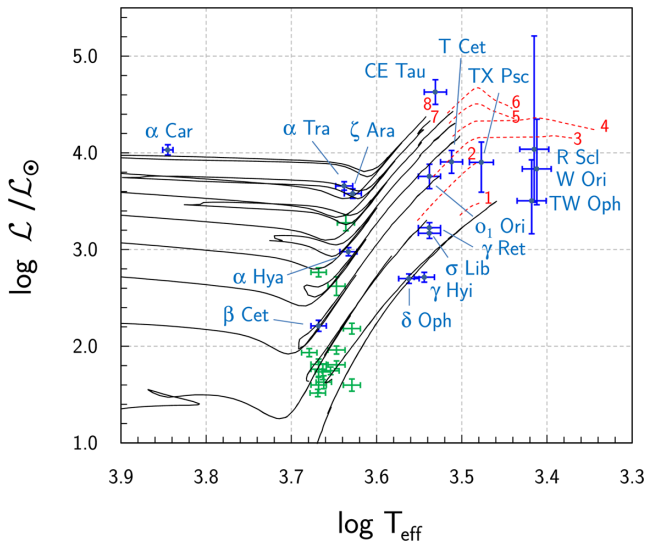

Figure 6. $T_{eff}-\mathcal{L}_{obs}$ diagram of the calibrators (thin green error bars) and science targets (thick blue error bars), with evolutionary tracks (black full lines) and AGBs (red dashed lines), for different masses, indicated in red at the end of each track.

9 TECHNETIUM

Technetium is an s-process element with no stable isotope and was first identified in the spectra of some M and S stars by Merrill (1952). With a laboratory half-life of 2.13×10^5 yr, the technetium isotope ^{99}Tc is the only one produced by the s-process in thermally-pulsating AGB (TP-AGB) stars (see Goriely & Mowlavi 2000). Due to the existence of an isomeric state of the ^{99}Tc nucleus, the high temperatures encountered during thermal pulses strongly shorten the effective half-life of ^{99}Tc ($t_{1/2} \sim 1$ yr at $\sim 3 \times 10^8$ K) (Cosner, Despain & Truran 1984), but the large neutron densities delivered by the ^{22}Ne$(\alpha,n)^{25}$Mg neutron source, operating at these high temperatures, more than compensate for the reduction of the ^{99}Tc lifetime (Mathews et al. 1986), and enable a substantial technetium produc-
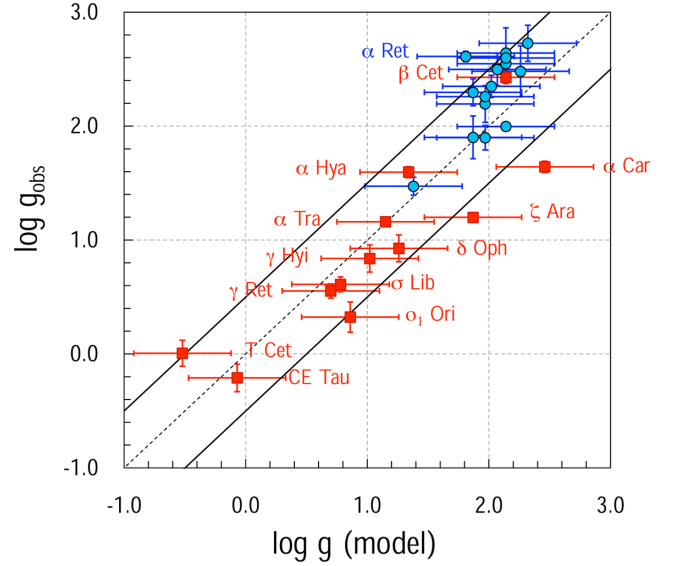
Figure 7. Comparison of the surface gravities used to select the MARCS models, with the values $\log g_{obs}$ derived from our final angular diameter value. Red squares: science targets; blue dots: calibrators. The solid lines mark the ±0.5 dex thresholds.

tion. The dredge-up episodes then carry technetium to the envelope, where it decays steadily at its terrestrial rate of $t_{1/2} = 2.13 \times 10^5$ yr. Starting from an abundance associated with the maximum observed in Tc-rich AGB stars, technetium should remain detectable during 1.0×10^6–1.5×10^6 yr (Smith & Lambert 1988). If the dredge-up of heavy elements occurs after each thermal pulse, occurring every 0.1×10^6–0.3×10^6 yr, virtually all s-process-enriched TP-AGB stars should exhibit technetium lines.

This conclusion applies to the situation where the s-process is powered by the ^{22}Ne$(\alpha,n)^{25}$Mg neutron source operating in the thermal pulse itself. However, Straniero et al. (1995) advocated that the s-process nucleosynthesis mainly occurs during the interpulse with neutrons from ^{13}C$(\alpha,n)^{16}$O (see Käppeler et al. 2011, for a recent review). When this process occurs in low-mass stars, and technetium is engulfed in the subsequent thermal pulse, it should not decay at a fast rate, because the arguments put forward by Cosner et al. (1984) and Mathews et al. (1986), and discussed above, only apply to intermediate-mass stars with hot thermal pulses.

One thus reaches the conclusion that *s-process-enriched* TP-AGB stars, of both low and intermediate mass, should necessarily exhibit technetium, unless the time span between successive dredge-ups becomes comparable to the Tc lifetime in the envelope. Indeed, all the S stars identified as TP-AGB stars by Van Eck et al. (1998), thanks to the *Hipparcos* parallaxes, turned out to be Tc rich, and a survey of technetium in the large Henize sample of S stars did not challenge that conclusion either (Van Eck & Jorissen 1999, 2000).

The present sample allows us to check whether a similar conclusion holds true for a sample comprising oxygen-rich giants and supergiants, as well as carbon stars. The technetium content of our science targets has been collected from the literature (last column of Table 1), and displayed in graphical form in Fig. 8 where it is confronted to the TP-AGB tracks (dashed lines) for different stellar masses. The presence or absence of Tc conforms to the expectations that namely TP-AGB stars exhibit Tc, except for the carbon star W Ori, where Tc has been tagged as absent by two independent studies, despite the fact that this star lies well within the TP-AGB region, as it should for a cool carbon star anyway. The s-process content
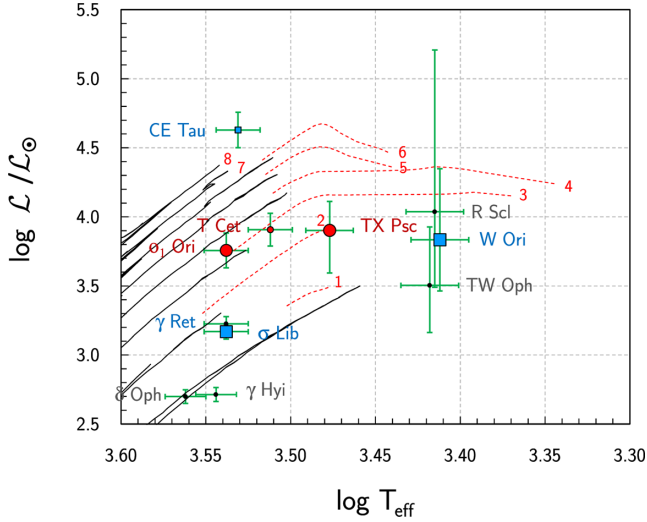
Figure 8. Same as Fig. 6, but restricted to the science targets, with their technetium content indicated. Large red circles: Tc present; small red circle: Tc probably present; large blue squares: Tc absent; small blue square: Tc doubtful; small black dots: unknown Tc content. Red dashed lines: TP-AGB tracks, for masses indicated at the end of each curve.

of that star has been studied by Abia et al. (2002) who find only moderate s-process enhancements, if any (≤ 0.3 dex), and this fact alone may explain the absence of detectable Tc. With the stellar parameters now available from our interferometric study for two more carbon stars (R Scl and TW Oph) falling in that region of the HRD, it will be of interest to perform a similar analysis on these two stars to get constraints on their nucleosynthesis processes.

10 PERIOD–LUMINOSITY RELATION

Since the present study derives radii and masses for some semi-regular variables, we also derive the pulsation constant Q (e.g. Fox & Wood 1982), defined as

$$Q = P \left(\frac{\mathcal{M}}{\mathcal{M}_\odot}\right)^{1/2} \left(\frac{\mathcal{R}_{\text{obs}}}{\mathcal{R}_\odot}\right)^{-3/2}, \qquad (5)$$

where P is the pulsation period given in Table 1. For pulsating stars with available periods of variation, we include Q in Table 6 (last column). Values of Q smaller than 0.04 d are typical of overtone pulsators (Fox & Wood 1982). Indeed, in the period–luminosity diagram (M_K, P) shown in Fig. 9, and following the terminology introduced by Wood (2000), most of these stars fall on the A', A and B overtone sequences, whilst only a few (TW Oph, TX Psc and R Scl) fall on the Mira fundamental-mode sequence C, despite the fact that these smaller amplitude carbon stars are actually classified as semi-regulars.

We note that masses should increase along each sequence, as predicted by theory (e.g. fig. 8 of Wood 1990). This is indeed the case, with our observed sample, with the exception of W Ori ($\mathcal{M} = 1.5\,\mathcal{M}_\odot$) and T Cet ($\mathcal{M} = 3\,\mathcal{M}_\odot$) along sequence B. Taking into account the large uncertainty of its bolometric magnitude, $M_{\text{bol}} = -5(1)$, derived from its absolute luminosity (Table 6), the location of the C-rich star W Ori on sequence B is rather uncertain. Using instead $M_{\text{bol}} = -4$ eliminates the problem, since it moves W Ori to its right position along sequence C, where the three other carbon stars of our sample are located.
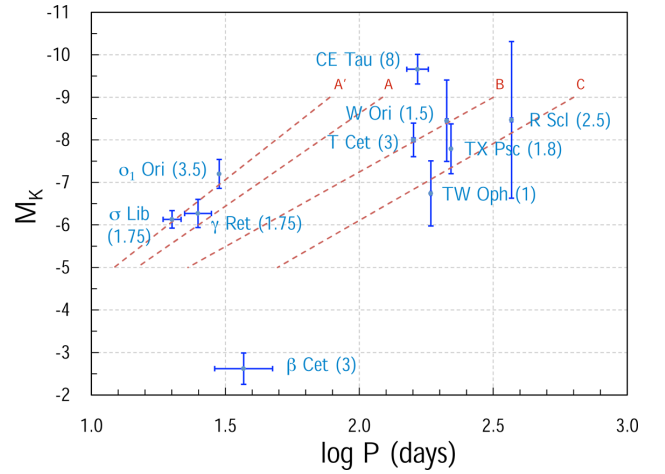

Figure 9. Period–luminosity diagram for science targets with available pulsation periods. M_K values are derived from the dereddened K magnitudes and the distance moduli. Stellar masses between parentheses (in $\mathcal{M}_\odot$). The location of the A' to C sequences is taken from Tabur et al. (2010).

11 CONCLUSION

We present new determinations of the angular diameter of a set of 10 O-rich giants, two supergiants and four C-rich giants, observed in the K band ($\mathcal{R} = 1500$) during several runs of a few nights, distributed over 2 years, using the VLTI/AMBER facility. They are obtained from the fit of synthetic SPI visibility and triple product on the true data. The synthetic SPI observables are derived by using a CLV profile calculated from MARCS model atmospheres.

We show that the results are moderately impacted (<1 per cent in angular diameter) by the variation of the model input parameters T_{eff}, $\log g$ and ξ_{turb}. During the observing period, using configurations covering different baseline angles, we find no significant variation of the angular diameter, except for TX Psc, a result which needs to be confirmed with complementary observations. For the eight targets previously measured by LBI in the same spectral band, our new angular diameter values are in good agreement with those of the literature. Except for TX Psc, the relative deviations between our values and those of the literature are less than 5 per cent, which validates our method. For TX Psc, a substantial temporal variation of the angular diameter, suspected to be correlated with the visual magnitude, could be invoked to account for the larger discrepancy. For the eight other targets, our values are first determinations, since no angular diameter measurements have been published yet for these stars.

These angular diameters are used to place the stars in the HRD and to derive their masses. For stars with a known technetium content, we confront their location in the HRD to the prediction that s-process nucleosynthesis producing technetium operates in TP-AGB stars. The two Tc-rich stars (o_1 Ori and TX Psc) indeed fall along the TP-AGB, as expected. However, the low-mass carbon-rich star W Ori, despite being located close to the top of the low-mass TP-AGB, has been flagged as devoid of Tc, which, if confirmed, would put interesting constraints on the s-process in low-mass carbon stars.

Finally, we compute the pulsation constant for the pulsating stars with available periods of variation. Their location along the pulsation sequences in the period–luminosity diagram confirms the mass dependency predicted by theory, except for W Ori and T Cet.

Those results, based on measurements of visibilities and triple products, illustrate the several ways to include LBI observations in the general investigation process in the field of stellar astrophysics.

ACKNOWLEDGEMENTS

REFERENCES

Abia C., Busso M., Gallino R., Domínguez I., Straniero O., Isern J., 2001, ApJ, 559, L1117

Abia C. et al., 2002, ApJ, 579, L817

Absil O. et al., 2010, A&A, 520, L2

Ake T. B., Johnson H. R., 1988, ApJ, 327, 214

Allen C. W., 2001, Allen's Astrophysical Quantities, 4th edn. Springer-Verlag, New York

Alvarez R., Plez B., 1998, A&A, 330, 1109

Amsler C. et al., 2008, Phys. Lett. B, 667, 1

Arenou F., Grenon M., Gomez A., 1992, A&A, 258, 104

Barnes T. G., Evans D. S., Moffett T. J., 1978, MNRAS, 183, 285

Baschek B., Scholz M., Wehrse R., 1991, A&A, 246, 374

Bastian U., Hefele H., 2005, in Turon C., O'Flaherty K. S., Perryman M. A. C., eds, The Three-Dimensional Universe with Gaia. ESA, Noordwijk, The Netherlands, p. 215

Beavers W. I., Cadmus R. R., Eitter J. J., 1982, AJ, 87, 818

Bedding T. R., Zijlstra A. A., von der Luhe O., Robertson J. G., Marson R. G., Barton J. R., Carter B. S., 1997, MNRAS, 286, 957

Bell R. A., Gustafsson B., 1989, MNRAS, 236, 653

Berdnikov L. N., Pavlovskaya E. D., 1991, SvA, 17, 215

Berio P. et al., 2011, A&A, 535, A59

Bertelli G., Girardi L., Marigo P., Nasi E., 2008, A&A, 484, 815

Bertelli G., Nasi E., Girardi L., Marigo P., 2009, A&A, 508, 355

Bevington P. R., Robinson D. K., 1992, Data Reduction and Error Analysis for The Physical Sciences. McGraw-Hill, New York, NY

Blackwell D. E., Shallis M. J., 1977, MNRAS, 180, 177

Blackwell D. E., Petford A. D., Shallis M. J., 1980, A&A, 82, 249

Blackwell D. E., Petford A. D., Arribas S., Haddock D. J., Selby M. J., 1990, A&A, 232, 396

Bordé P., Coudé du Foresto V., Chagnon G., Perrin G., 2002, A&A, 393, 183

Brown T. M., Christensen-Dalsgaard J., 1998, ApJ, 500, L195

Chen B., Vergely J. L., Valette B., Carraro G., 1998, A&A, 336, 137

Chiavassa A. et al., 2011, A&A, 528, A120

Cohen M., Walker R. G., Carter B., Hammersley P., Kidger M., Noguchi K., 1999, AJ, 117, 1864

Cosner K. R., Despain K. H., Truran J. W., 1984, ApJ, 283, L313

Cruzalèbes P., Spang A., Sacuto S., 2008, in Kaufer A., Kerber F., eds, The 2007 ESO Instrument Calibration Workshop, Calibration of AMBER Visibilities at Low Spectral Resolution. Springer-Verlag, Berlin Heidelberg, Germany, p. 479

Cruzalèbes P., Jorissen A., Sacuto S., Bonneau D., 2010, A&A, 515, A6

Cruzalèbes P. et al., 2013a, MNRAS, 432, 1658

Cruzalèbes P. et al., 2013b, MNRAS, submitted

Currie D. G., Knapp S. L., Liewer K. M., Braunstein R. H., 1976, Stellar dD dDiameter Measurements by Amplitude Interferometry 1972–1976. Dept. Phys. Astron., Univ. Maryland, MA

de Jager C., Nieuwenhuijzen H., 1987, A&A, 177, 217

de Vegt C., 1974, A&A, 34, 457

Decin L., Vandenbussche B., Waelkens K., Eriksson C., Gustafsson B., Plez B., Sauval A. J., 2003, A&A, 400, 695

Dehaes S., Groenewegen M. A. T., Decin L., Hony S., Raskin G., Blommaert J. A. D. L., 2007, MNRAS, 377, 931

Domiciano de Souza A., Bendjoya P., Vakili F., Millour F., Petrov R. G., 2008, A&A, 489, L5

Drimmel R., Spergel D. N., 2001, ApJ, 556, L181

Dumm T., Schild H., 1998, New Astron., 3, 137

Dunham D. W., Evans D. S., Silverberg E. C., Wiant J. R., 1975, MNRAS, 173, 61p

Duvert G., Chelli A., Malbet F., Kern P., 2010, A&A, 509, A66

Dyck H. M., Benson J. A., van Belle G. T., Ridgway S. T., 1996, AJ, 111, 1705

Dyck H. M., van Belle G. T., Benson J. A., 1996, AJ, 112, 294

Dyck H. M., van Belle G. T., Thompson R. R., 1998, AJ, 116, 981

Efron B., 1979, Ann. Statist., 7, 1

Efron B., 1982, The Jacknife, the Bootstrap, and other Resampling Plans. SIAM-NF-CBMS, Philadelphia, PA

Enders G. K., 2010, Applied Missing Data Analysis. Guilford Press, New York, NY

Engelke C. W., Price S. D., Kraemer K. E., 2006, AJ, 132, 1445

Eriksson U., Lindegren L., 2007, A&A, 476, 1389

Eriksson K., Linsky J. L., Simon T., 1983, ApJ, 272, L665

Fitzgerald M. P., 1968, AJ, 73, 983

Fox M. W., Wood P. R., 1982, ApJ, 259, L198

Gai M. et al., 2004, in Traub W. A., ed., SPIE Conf. Ser. Vol. 5491, New Frontiers in Stellar Interferometry. SPIE, Bellingham, WA, p. 528

Goodman J. W., 1985, Statistical Optics. Wiley Classics Library, New York, NY

Goriely S., Mowlavi N., 2000, A&A, 362, 599

Gray D. F., 2005, The Observation and Analysis of Stellar Photospheres, 3rd edn. Cambridge Univ. Press, Cambridge, UK

Gustafsson B., Edvardsson B., Eriksson K., Jørgensen U. G., Nordlund Å., Plez B., 2008, A&A, 486, 951

Hakkila J., Myers J. M., Stidham B. J., Hartmann D. H., 1997, AJ, 114, 2043

Hanbury Brown R., Davis J., Allen L. R., Rome J. M., 1967, MNRAS, 137, 393

Hanbury Brown R., Davis J., Allen L. R., 1974, MNRAS, 167, 121

Hertzsprung E., 1922, Ann. Sterrew. Leiden, 14, A1

Houk N., 1978, Michigan Catalogue of Two-dimensional Spectral Types for the HD stars. Univ. Michigan, Ann Arbor, MI

Houk N., Cowley A. P., 1975, University of Michigan Catalogue of Two-dimensional Spectral Types for the HD stars. Vol. 1. Declinations −90°.0 to −53°.0. Univ. Michigan, Ann Arbor, MI

Houk N., Smith-Moore M., 1988, Michigan Catalogue of Two-dimensional Spectral Types for the HD Stars. Vol. 4. Declinations −26°.0 to −12°.0. Univ. Michigan, Ann Arbor, MI

Huber P. J., Ronchetti E. M., 2009, Robust Statistics. Wiley, Hoboken, NJ

JCGM-WG1, 2008, Evaluation of Measurement Data - Guide to the Expression of Uncertainty in Measurement. BIPM, Paris, France

Johnson H. M., Wright C. D., 1983, ApJS, 53, 643

Judge P. G., Stencel R. E., 1991, ApJ, 371, L357

Käppeler F., Gallino R., Bisterzo S., Aoki W., 2011, Rev. Mod. Phys., 83, 157

Kelley K., 2007, J. Statistic. Softw., 20, 1

Kholopov P. N. et al., 1998, Combined General Catalogue of Variable Stars, 4.1 edn (II/214A). Sternberg Institute, Sweden

Knapp G. R., Pourbaix D., Platais I., Jorissen A., 2003, A&A, 403, 993

Lafrasse S., Mella G., Bonneau D., Duvert G., Delfosse X., Chesneau O., Chelli A., 2010, in Danchi W. C., Delplancke F., Rajagopal J. K., eds, SPIE Conf. Ser. Vol. 7734, Optical and Infrared Interferometry II. SPIE, Belligham, WA, p. 140

Lambert D. L., Gustafsson B., Eriksson K., Hinkle K. H., 1986, ApJS, 62, 373

Landi Dessy J., Keenan P. C., 1966, ApJ, 146, L587

Le Bouquin J., Bauvir B., Haguenauer P., Schöller M., Rantakyrö F., Menardi S., 2008, A&A, 481, 553

Lebzelter T., Hron J., 1999, A&A, 351, 533

Lebzelter T., Hron J., 2003, A&A, 411, 533

Leggett S. K., Mountain C. M., Selby M. J., Blackwell D. E., Booth A. J., Haddock D. J., Petford A. D., 1986, A&A, 159, 217

Lindegren L. et al., 2008, in Jin W. J., Platais I., Perryman M. A. C., eds, Proc. IAU Symp. 248, A Giant Step: from Milli- to Micro-arcsecond Astrometry. Cambridge Univ. Press, Cambridge, UK, p. 217

Little S. J., Little-Marenin I. R., Bauer W. H., 1987, AJ, 94, 981

Maercker M. et al., 2012, Nat, 490, 232

Marquardt D. W., 1963, Indian J. Indust. Appl. Math., 11, 431

Mason B. D., Wycoff G. L., Hartkopf W. I., Douglass G. G., Worley C. E., 2001, AJ, 122, 3466

Mathews G. J., Takahashi K., Ward R. A., Howard W. M., 1986, ApJ, 302, L410

Merrill S. P. W., 1952, ApJ, 116, L21

Michelson A. A., Pease F. G., 1921, ApJ, 53, L249

Millan-Gabet R., Pedretti E., Monnier J. D., Schloerb F. P., Traub W. A., Carleton N. P., Lacasse M. G., Segransan D., 2005, ApJ, 620, L961

Montes D., López-Santiago J., Gálvez M. C., Fernández-Figueroa M. J., De Castro E., Cornide M., 2001, MNRAS, 328, 45

Morbey C. L., Fletcher J. M., 1974, Publ. Dom. Astrophys. Obs., 14, 271

Morgan W. W., Keenan P. C., 1973, ARA&A, 11, 29

Mozurkewich D. et al., 2003, AJ, 126, 2502

Neckel T., Klare G., 1980, A&AS, 42, 251

Ochsenbein F., Halbwachs J. L., 1982, A&AS, 47, 523

Ohnaka K. et al., 2005, A&A, 429, 1057

Otero S. A., Moon T., 2006, J. Am. Assoc. Variable Star Obs., 34, 156

Pasinetti Fracassini L. E., Pastori L., Covino S., Pozzi A., 2001, A&A, 367, 521

Pasquato E., Pourbaix D., Jorissen A., 2011, A&A, 532, A13

Perryman M. A. C. et al., 2001, A&A, 369, 339

Plez B., 2012, Astrophysics Source Code Library, record ascl : 1205.004

Press W. H., Teukolsky S. A., Vetterling W. T., Flannery B. P., 2007, Numerical Recipes. The Art of Scientific Computing, 3rd edn. Cambridge Univ. Press, Cambridge, UK

Quirrenbach A., Mozurkewich D., Armstrong J. T., Buscher D. F., Hummel C. A., 1993, ApJ, 406, L215

Quirrenbach A., Mozurkewich D., Hummel C. A., Buscher D. F., Armstrong J. T., 1994, A&A, 285, 541

Ragland S. et al., 2006, ApJ, 652, L650

Ramstedt S., Schöier F. L., Olofsson H., 2009, A&A, 499, 515

Richichi A., di Giacomo A., Lisi F., Calamai G., 1992, A&A, 265, 535

Richichi A., Chandrasekhar T., Lisi F., Howell R. R., Meyer C., Rabbia Y., Ragland S., Ashok N. M., 1995, A&A, 301, 439

Richichi A., Percheron I., Khristoforova M., 2005, A&A, 431, 773

Richichi A., Percheron I., Davis J., 2009, MNRAS, 399, 399

Ridgway S. T., Wells D. C., Joyce R. R., 1977, AJ, 82, 414

Ridgway S. T., Jacoby G. H., Joyce R. R., Wells D. C., 1980, AJ, 85, 1496

Ridgway S. T., Jacoby G. H., Joyce R. R., Siegel M. J., Wells D. C., 1982, AJ, 87, 808

Rowan-Robinson M., Lock T. D., Walker D. W., Harris S., 1986, MNRAS, 222, 273

Sacuto S., Aringer B., Hron J., Nowotny W., Paladini C., Verhoelst T., Höfner S., 2011, A&A, 525, A42

Scargle J. D., Strecker D. W., 1979, ApJ, 228, L838

Scholz M., 1997, in Bedding T. R., Booth A. J., Davis J., eds, Proc. IAU Symp. 189, Stellar Radii. Kluwer, Dordrecht, The Netherlands, p. 51

Skrutskie M. F. et al., 2006, AJ, 131, 1163

Slee O. B., Stewart R. T., Bunton J. D., Beasley A. J., Carter B. D., Nelson G. J., 1989, MNRAS, 239, 913

Smalley B., 2005, Mem. Soc. Astron. Ital. Suppl., 8, 130

Smith V. V., Lambert D. L., 1985, ApJ, 294, L326

Smith V. V., Lambert D. L., 1988, ApJ, 333, L219

Smithson M. J., 2002, Confidence Intervals. Sage Publications, Thousand Oaks, CA

Straniero O., Gallino R., Busso M., Chiefei A., Raiteri C. M., Limongi M., Salaris M., 1995, ApJ, 440, L85

Tabur V., Bedding T. R., Kiss L. L., Giles T., Derekas A., Moon T. T., 2010, MNRAS, 409, 777

van Belle G. T., Dyck H. M., Benson J. A., Lacasse M. G., 1996, AJ, 112, 2147

van Belle G. T. et al., 1999, AJ, 117, 521

Van Eck S., Jorissen A., 1999, A&A, 345, 127

Van Eck S., Jorissen A., 2000, A&A, 360, 196

Van Eck S., Jorissen A., Udry S., Mayor M., Pernier B., 1998, A&A, 329, 971

van Leeuwen F., 2007, A&A, 474, 653

Wasatonic R. P., 1997, J. Am. Assoc. Variable Star Obs., 26, 1

Watson C. L., Henden A. A., Price A., 2006, The International Variable Star Index (VSX). Society for Astronomical Science, Pittsburg, CA

Wesselink A. J., Paranya K., DeVorkin K., 1972, A&AS, 7, 257

White N. M., 1980, ApJ, 242, L646

White N. M., Kreidl T. J., Goldberg L., 1982, ApJ, 254, L670

Winzer P., 2000, Rev. Sci. Instrum., 71, 1447

Wood P. R., 1990, in Mennessier M. O., Omont A., eds, From Miras to Planetary Nebulae: Which Path for Stellar Evolution? Pulsation and Evolution of Mira Variables. Atlantica Séguier Frontières, Gif sur Yvette, France, p. 67

Wood P. R., 2000, PASA, 17, 18

Yudin R. V., Evans A., 2002, A&A, 391, 625

This paper has been typeset from a TEX/LATEX file prepared by the author.